Preferred citation: S. Ramaswamy, S. Huang, A. Goel, A. Cooper, D. Choi, A Bandyopadhyay and B.V. Ramarao. The 3D Structure of Paper and its Relationship to Moisture Transport in Liquid and Vapor Forms. In **The science of papermaking**, *Trans. of the XIIth Fund. Res. Symp. Oxford, 2001*, (C.F. Baker, ed.), pp 1289–1311, FRC, Manchester, 2018. DOI: 10.15376/frc.2001.2.1289.

THE 3D STRUCTURE OF PAPER AND ITS RELATIONSHIP TO MOISTURE TRANSPORT IN LIQUID AND VAPOR FORMS

Shri Ramaswamy,[1*] *Shuiyuan Huang,*[1] *Amit Goel,*[1] *Aron Cooper,*[1] *Doeung Choi,*[2] *A. Bandyopadhyay*[3] *and B. V. Ramarao*[3]

[1]Department of Wood and Paper Science, College of Natural Resources, University of Minnesota, St. Paul, MN 55108. USA.
[2]Hercules Research Center, Hercules Inc., Wilmington DE, USA.
[3]Faculty of Paper Science and Engineering and Empire State Paper Research Institute, SUNY College of Environmental Science and Forestry, Syracuse NY 13210. USA.

ABSTRACT

The three dimensional structure of paper materials plays a critical role in the paper manufacturing process especially via its impact on the transport properties for fluids. Dewatering of the wet web, pressing and drying will benefit from knowledge of the relationships between the web structure and its transport coefficients. Among transport, moisture diffusion in paper is central to the understanding and optimal design of paper products for their performance in different environmental conditions. Our recent research of moisture sorption in paper has indicated that diffusion of water vapor through the pore space is an important mechanism for transport [1,2]. The effect of the three dimensional structure of the paper sheet on the diffusion of moisture is significant.

The structure of the pore space within a paper sheet is imaged

in serial sections using x-ray microtomography. The three dimensional structure is reconstructed from these sections using digital image processing techniques. The structure is then analyzed by measuring traditional descriptors for the pore space such as specific surface area and porosity. In addition, morphometric and quantitative stereological techniques are used to characterize the structure. Techniques of mathematical morphology [3] used include erosion, dilation, closing, opening and binarization with subsequent skeletonization.

A sequence of microtomographs was imaged at approximately 2 μm intervals and the three-dimensional pore-fiber structure was reconstructed. The pore size distributions for both in-plane as well as transverse pores were measured. Significant differences in the in-plane (X-Y) and the transverse directions in pore characteristics are found and may help partly explain the different liquid and vapor transport properties in the in-plane and transverse directions. The results from the mathematical morphological study show that the pore space and the fiber space are bicontinuous. Some network measures of both these spaces are the network nodal density and bond co-ordination number distribution, both of which are determined. Significant transport properties for the pore space include the saturated water permeability and water vapor diffusivity. Due to the anisotropic nature of the structure, these are three-dimensional tensors in general.

INTRODUCTION

The structure of the inter-fiber voids in paper governs some of its important transport properties. Among the most significant is the conductivity to moisture in both the saturated and unsaturated states. Moisture conduction in free liquid, bound water and vapor forms is central to many processing operations such as the drainage of the wet-web, its subsequent dewatering under vacuum and pressure and finally its drying behavior. Furthermore, conductivity of the paper to moisture at low moisture contents is important in controlling the physical properties such as its elastic moduli [4,5]. Thus, the relationship between the structure of the paper from the void space and fiber aspects is of significant interest.

X-ray microtomography is a relatively new technique used in the three-dimensional imaging of materials. This method consists of obtaining large

set of images while passing radiation through the sample at different angles. The projected images can be combined to reconstruct an approximation of geometry of the interior structure. Traditional x-ray imaging in medical applications uses absorptive contrast between high density bone materials and low density tissue. In the case of paper and board, cellulose and the surrounding medium have approximately equal absorptivities and hence the contrast is minimal. In such structures, "phase contrast imaging" based on relative difference in refractive index between cellulose fibers and surrounding medium is used. Samuelsen et.al. [6,7], Guruyev et.al. [8], Goel et al. [12] have shown the use of "phase contrast imaging" in paper.

In order to study the relationship between pore structure and transport properties, hand sheets of varying structure were prepared by subjecting bleached soft wood kraft fibers to varying degrees of refining. The level of mechanical pressing and other sheet forming variables were held constant. The change in apparent density values for the samples did indicate potential change in internal structure. Shown below are example microtomographs of specimens of paper sheets refined to different degrees of freeness in the laboratory.

The X-ray images were then binarized to distinguish fiber and voids using a *dynamic thresholding method* [9,13]. This method is based on the fact that the threshold value of a pixel depends on the intensities of the neighboring pixels. Each image was divided into number of overlapping windows of 128×128 pixels. Threshold values for the pixels at the center of each window were calculated using the *minimum error thresholding method* [10,13]. This method tries to minimize the probability of misclassifying a pixel. Based on the pixel values, an intensity histogram was computed over each window. Histograms obtained using these methods were bi-modal with one distribution corresponding to voids and other to fibers. A sample histogram is shown in Figure 3. Threshold values were then calculated for pixels at the center of each window using an iterative procedure. After the threshold values for the pixels at the center of each window were calculated, thresholds for the remaining pixels were calculated using bilinear interpolation. Finally, the original intensity value g(m,n) was compared with the threshold value T(m,n) for each pixel, where (m,n) are the pixel coordinates. If $g(m,n) > T(m,n)$ a value of 1 was assigned to the pixel, otherwise, the pixel intensity was set to 0.

Having identified the fiber (white, pixel intensity 1) and void (black, pixel intensity 0), the traditional pore structure descriptors such as porosity and specific surface area are calculated as follows. The porosity (ε) of the total sample is calculated by taking the ratio of the total void pixels and the total sample pixels. The three dimensional void structure was reconstructed from a sequence of closely spaced images (2 μm apart between the serial sections).

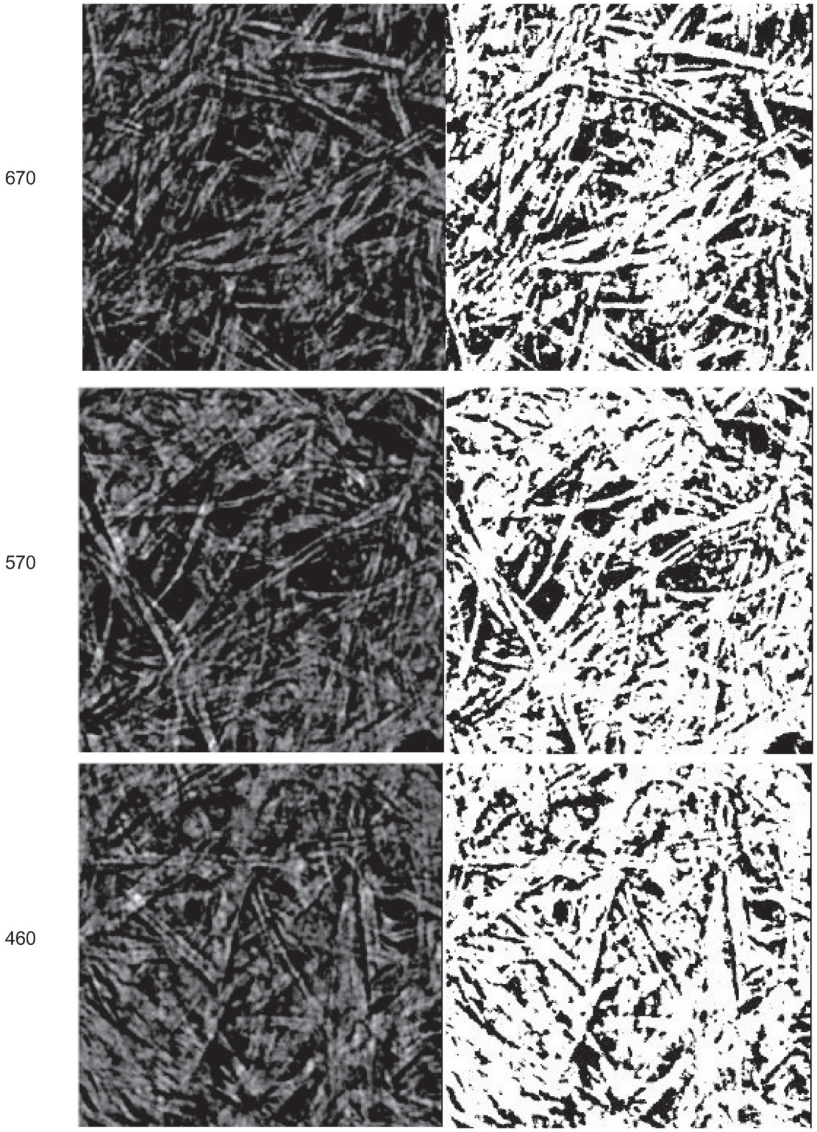
670
570
460

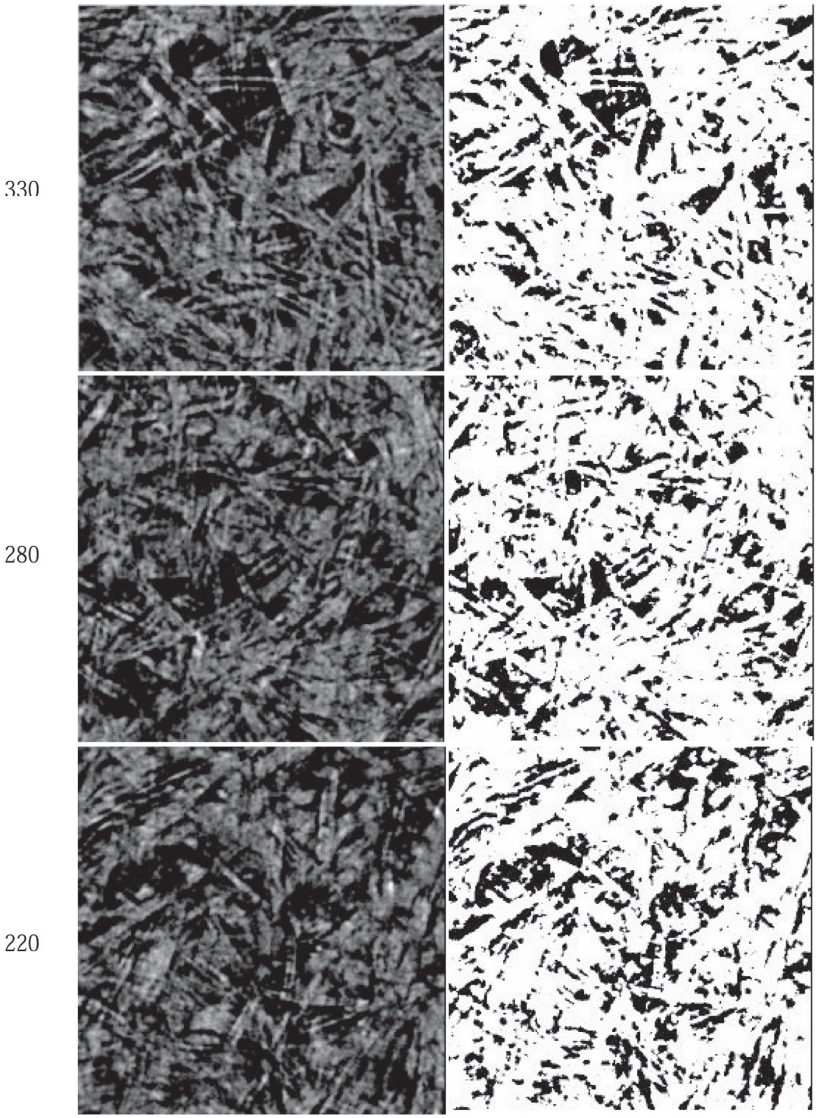

Figure 1 X-ray microtomograph images of paper sheet specimens in the X-Y plane at 6 different refining levels (670, 570, 460, 330, 280, 220 CSF). Binary images corresponding to each image are shown in the right column.

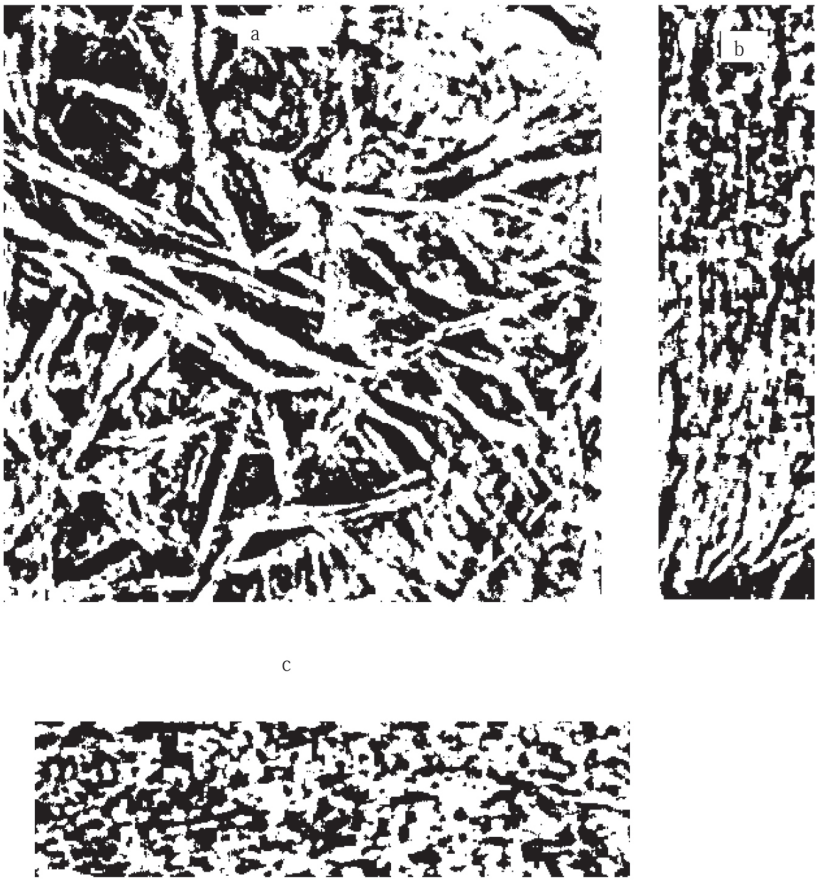

Figure 2 Binarized version of the microtomograph sections in the (a) X-Y, (460 × 460 pixels) (b) Y-Z (120 × 460 pixels) and (c) X-Z (460 × 120 pixels) planes.

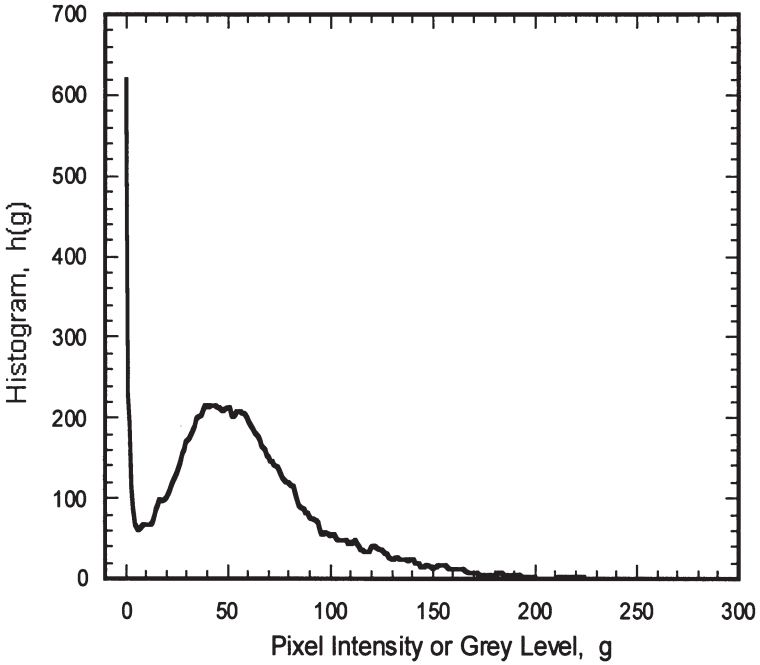

Figure 3 Sample histogram for one of the windows.

This gave the void surface in the third dimension. A pixel when projected into the third dimension forms a voxel. Each of the fiber voxels was then compared with all of its adjacent neighbors to identify the fiber-void interfacial area. The specific surface area is then calculated as,

$$S_w = \frac{S_t}{(1-\varepsilon)\rho_f} \tag{1}$$

The specific surface area is given in m^2/g, the total interfacial area from the voxels is S_t, m^2, the fiber density is denoted by ρ_f (g/m^3). The porosity and specific surface area calculated from micro X-ray tomography and image analysis for samples of varying structure is shown in Figure 4. As one would expect, the porosity of the samples decrease with increasing refining or decreasing freeness values. It is interesting to note, however, that the major decrease in porosity is from larger pores (pores greater than 4.0 microns in diameter), as shown by mercury intrusion porosimetry data on these samples

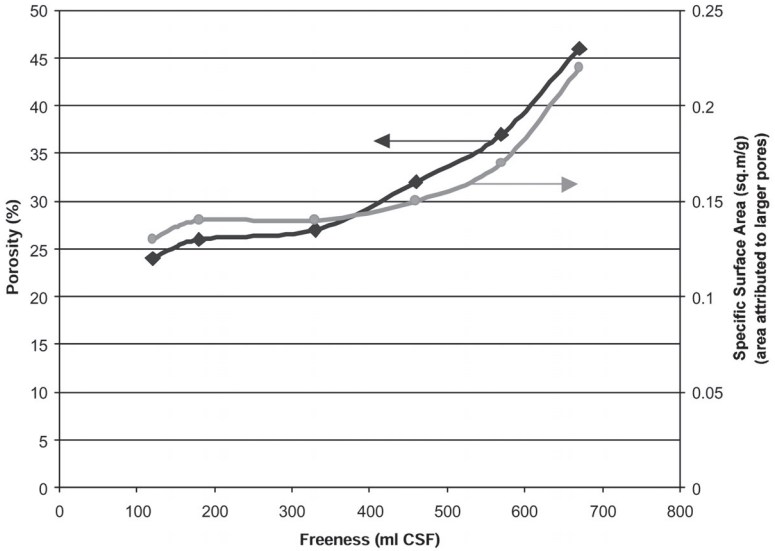

Figure 4 Porosity and specific surface area from X-ray tomography and image analysis for samples of varying structure.

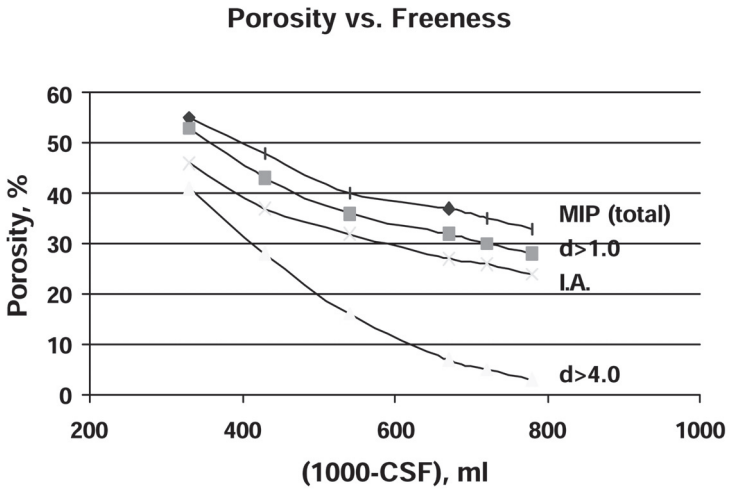

Figure 5 Porosity comparison between Image Analysis and Mercury Intrusion Porosimetry (MIP) for samples of varying structure.

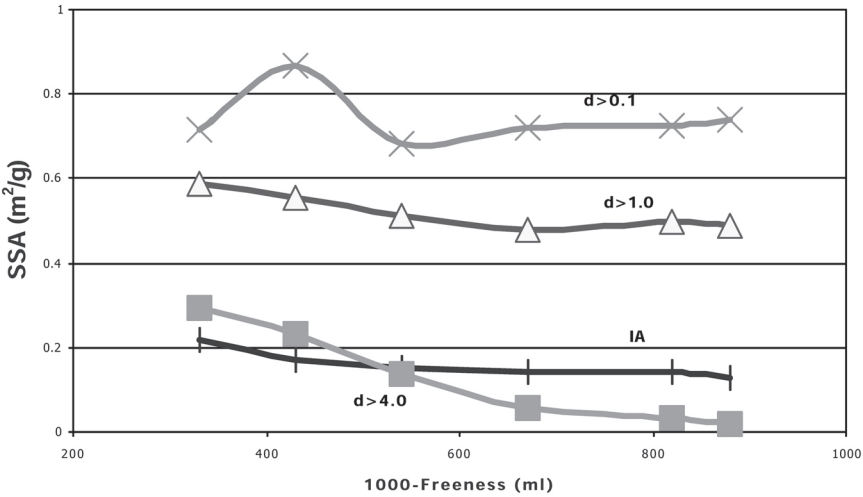

Figure 6 Specific surface area comparison between Image Analysis and Mercury Intrusion Porosimetry (MIP) for samples of varying structure.

(Figure 5). The specific interface area was also found to decrease with freeness. At first this appears contradictory. Normally one would expect the specific surface area to increase with refining. This was indeed the case when one looks at the total specific surface area as measured by the traditional mercury intrusion technique. However, the specific surface area of pores greater than 1.0 micron in diameter was found to decrease with refining, a trend similar to that observed with image analysis (Figure 6). Detailed analysis of the mercury intrusion porosimetry data shows that while the major decrease in pore volume comes from larger pores (pore diameter > 4.0 microns), the increase in surface area with refining is primarily from much smaller pores (pore diameter less than 0.1 microns). This explains why the image analysis data show a decrease in porosity as well as a decrease in surface area with refining. Porosity and specific surface area distributions as a function of pore diameter as obtained by mercury intrusion porosimetry for the slightly refined and highly refined samples are shown in Figures 7 and 8 [11].

In addition to porosity and specific surface area, another traditional descriptor used in porous media is the distribution of pore size. Techniques such as mercury intrusion porosimetry generally give the volume distribution corresponding to the entire sample (Figure 7 and Figure 8). Using X-ray and image analysis, it is possible to evaluate the pore size distribution in the three

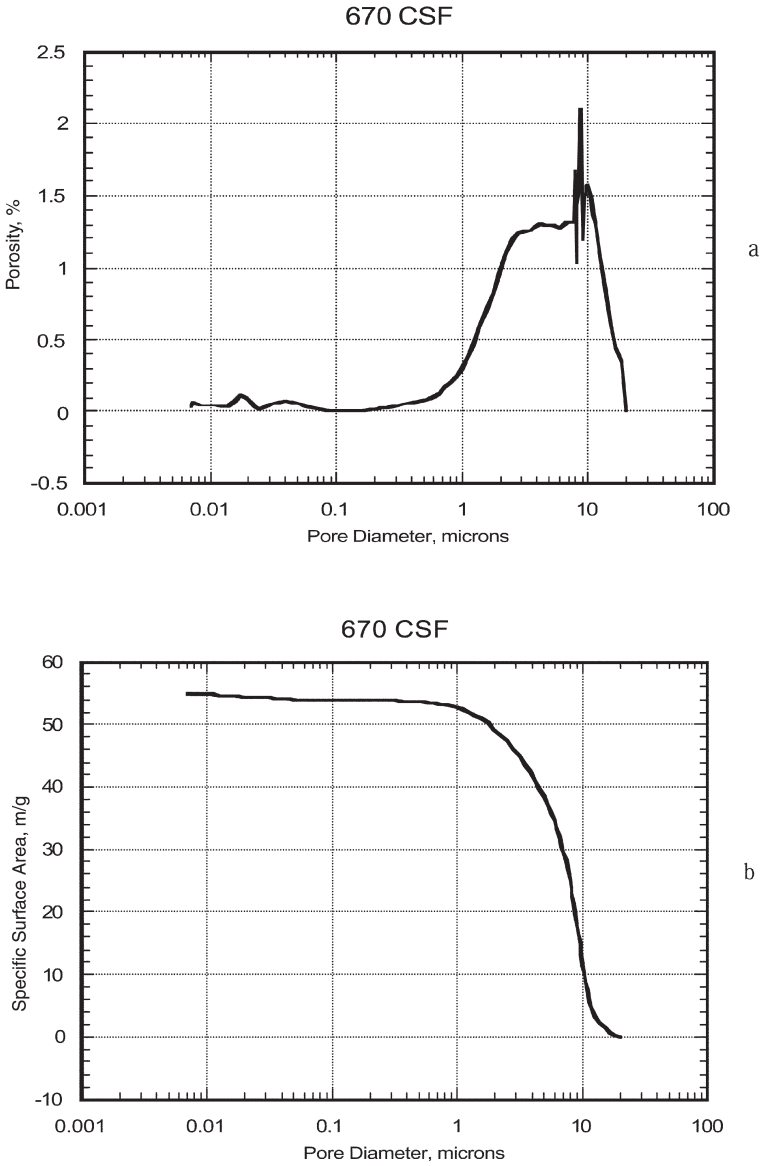

Figure 7 Porosity (a), Cumulative Porosity (b), Specific Surface Area (c), and Cumulative Specific Surface Area (d) distributions by Mercury Intrusion Porosimetry for 670 CSF sample.

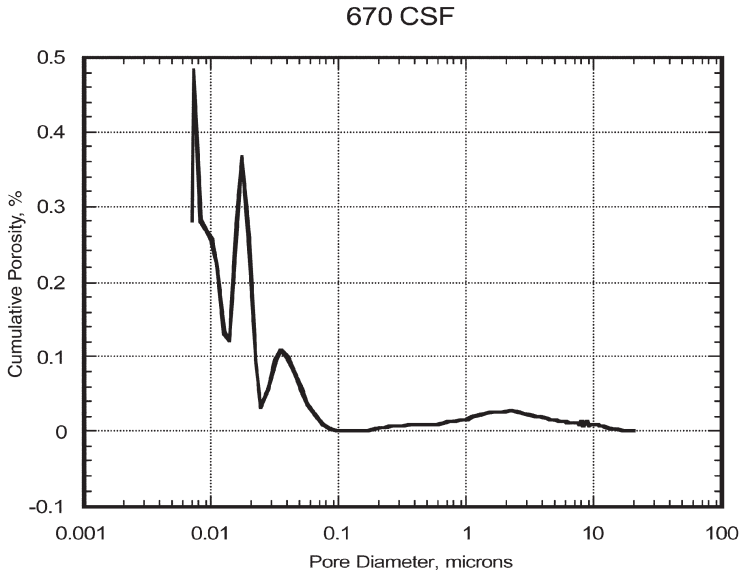

c

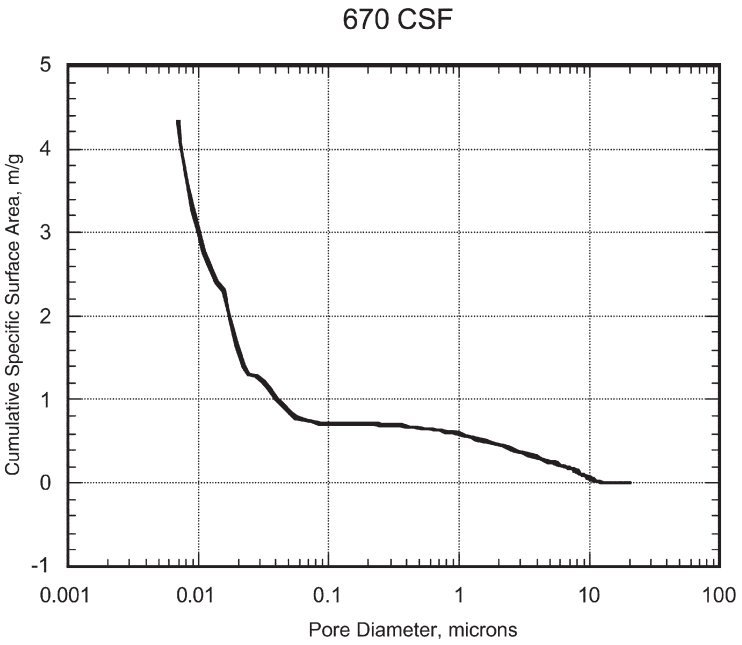

d

Figure 7 Continued.

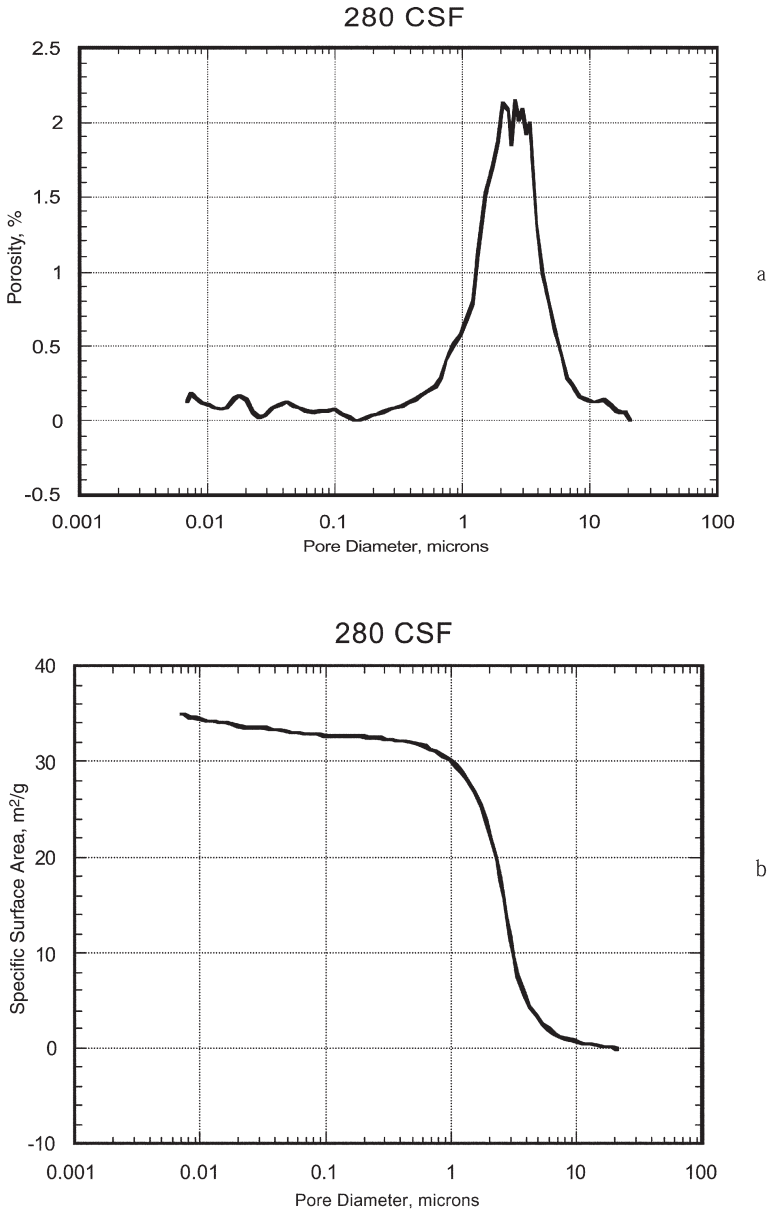

Figure 8 Porosity (a), Cumulative Porosity (b), Specific Surface Area (c), and Cumulative Specific Surface Area (d) distributions by Mercury Intrusion Porosimetry for 280 CSF sample [11].

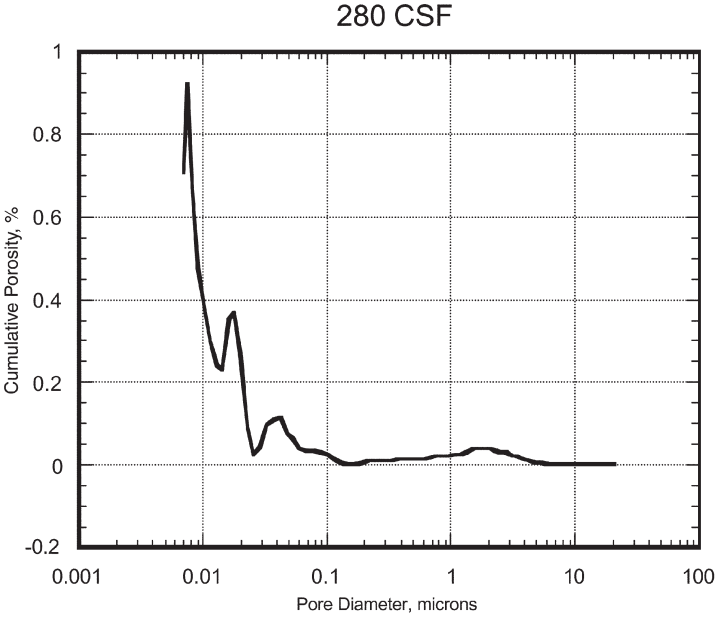

c

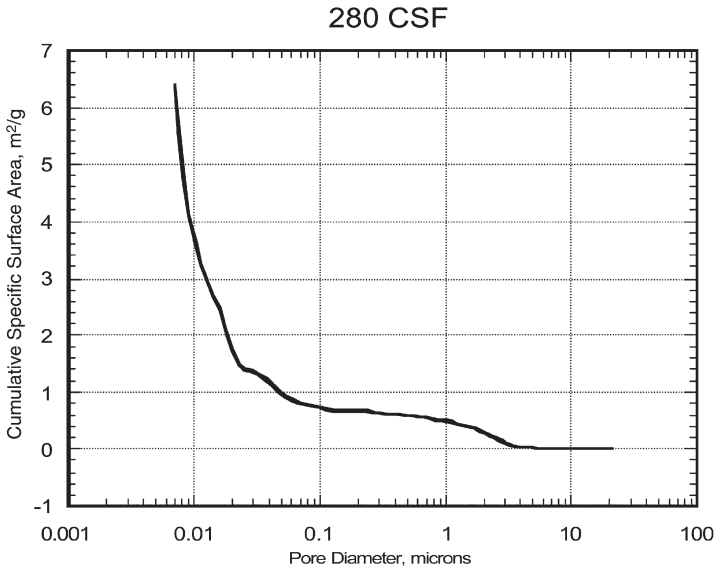

d

Figure 8 Continued.

independent directions. Such pore size distribution will be more meaningful in analyzing fluid flow predominantly in one direction, i.e. in-plane flow, transverse flow. In order to conduct such analysis, we define pore hydraulic radius ($R_{p,h}$, m) as follows:

$$R_{p,h} = \frac{A_p}{W_p} \tag{2}$$

where A_p is the cross sectional area of a pore (m^2) and W_p is its perimeter (m). Since the pores can be identified from contiguous white or black regions in a binarized image, the pore size distribution can be estimated easily. Having identified the pores and their areas in each plane through the entire thickness, the perimeter of each pore is then calculated by identifying the set of pixels that belong to the pore and that have at least one neighbor that interfaces with a fiber pixel.

The volume of each pore identified in any given plane is calculated by

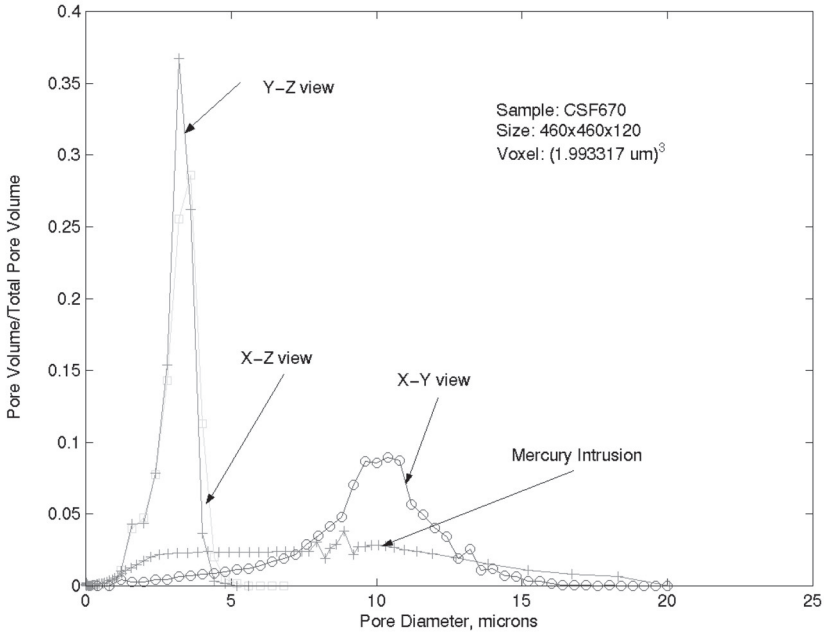

Figure 9 Comparison of pore size distribution in the XY, YZ and XZ planes by image analysis and the mercury intrusion method for unrefined (670 CSF).

multiplying the area of that pore by the constant slice thickness. By stacking up the volume occupied by pores of a given hydraulic radius for all slices through the thickness in any given plane, the overall pore size distribution in any plane for a sample can be obtained. It is assumed that the total pore volume (or porosity) in any given sample is the same irrespective of the XY, YZ, or XZ plane of view. Figures 9 and 10 show the pore size distribution obtained by image analysis in the XY, YZ and XZ views for two different structures. For comparison the overall pore size distribution obtained by traditional mercury intrusion porosimetry is also shown in the same figure. Here, normalized pore volumes obtained by dividing the pore volume corresponding to a specific pore size by the total pore volume is represented on the y-axis. It is interesting to note that for any given structure, the pore size distribution in the XY (or transverse) view is broader than the YZ or XZ views (in-plane views). The average pore size in the XY view is also larger than the other two directions. This indicates that potentially the fluid flowing

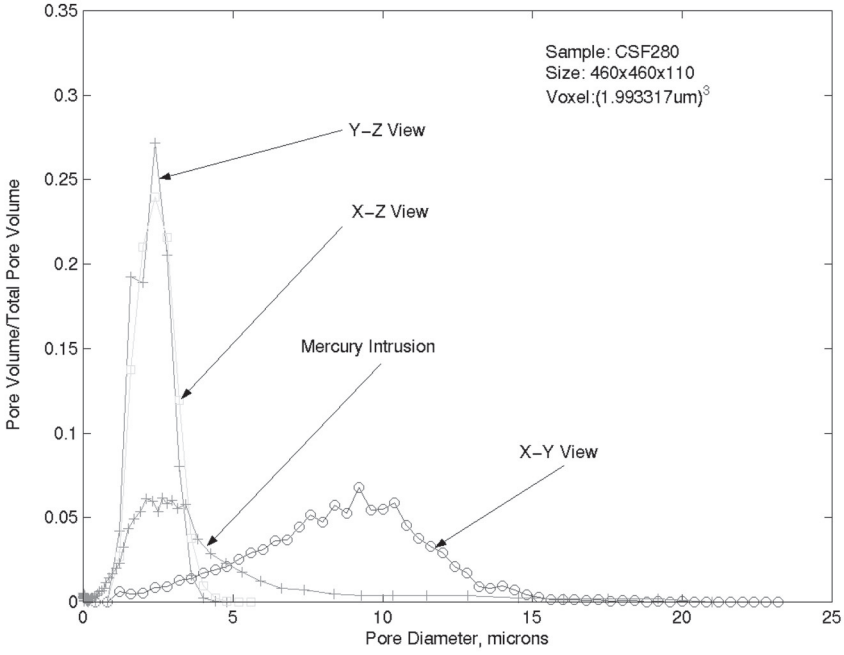

Figure 10 Comparison of pore size distribution in the XY, YZ and XZ planes by image analysis and the mercury intrusion method for highly refined pulp (280 CSF).

in the transverse direction encounters a much more open pore structure with larger pore sizes compared to the in-plane direction. This may help partly explain the differences observed in in-plane vs transverse permeability experiments.

As we go from a slightly refined to highly refined sample (Figure 9 vs Figure 10), the overall pore volume has decreased, as indicated earlier by the porosity values. Also, the pore size distribution shifts towards smaller pore size. But, the distinct difference between in-plane and transverse views is still very much present. The pore size distribution by mercury intrusion, on the other hand, cannot distinguish between the in-plane and transverse views. The mercury intrusion data indicate the narrowing of the pore size distribution with refining, shifting towards the smaller pore size. The pore size distribution by mercury intrusion is more close to the XY view than the other two views. One difference between the X-ray, image analysis and the mercury intrusion technique is that due to the lower resolution of the X-ray technique (~3–4 microns), we are unable to visualize the very small pores in the original image. As a result, the pore volume distribution obtained by mercury intrusion at the small pore size ranges are higher than that obtained by X-ray and image analysis. It is possible that with a higher resolution technique (~1 micron), such as the one used by Samuelsen et al. [6,7] or Gureyev et al. [8] more accurate distributions at the lower pore sizes can be obtained.

Pore-bond Network Representations

In addition to traditional pore structure analysis using conventional measures such as porosity, specific surface area, pore size distribution morphometric and other quantitative stereological techniques have been used to analyze the three dimensional structure. In this paper, we restrict our attention to the two-dimensional case and consider the three dimensionality in a subsequent report. First, the bi-level images obtained in each of the XY, YZ and XZ planes through the thickness of a given sample are skeletonized by sequential erosion operations without effecting pore connectivity. The skeletonization procedure can be used to minimize either the fiber or the void area to just a single line of pixels representing the original image. Skeletons of fibers and voids overlaid on the original binarized image using Matlab™ Image Toolkit are shown in Figures 11 and 12. It is interesting to note that the skeletons, in both figures, very closely represent the original fiber and void structure. It should be pointed out that no smoothing algorithm was used in the original bi-level image. As a result, the fiber-void interface is rough with a number of small projections. The skeletons, to some extent, misrepresent some of these projections as short pathways attached to the backbone. A higher resolution

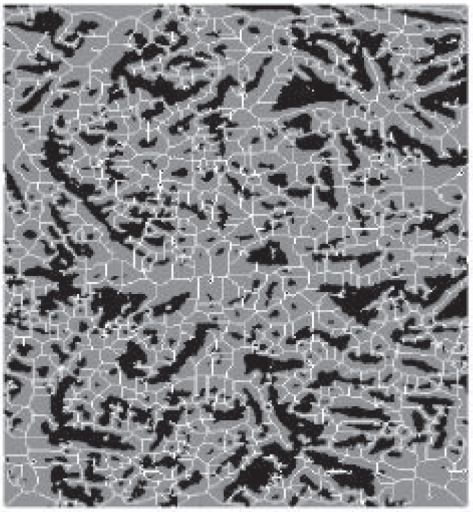

Figure 11 Skeleton of fiber over laid on binarized image.

Figure 12 Skeleton of pores over laid on binarized image.

X-ray imaging technique in combination with a smoothing algorithm is expected to eliminate some of the rough interfaces and the artifices on the skeleton.

The network structure represented by the skeleton can now be quantitatively described using network nodal density, co-ordination number and bond length distributions. Nodes are defined as points or pixels at which two or more bonds intersect. Skeleton branches coming off a main backbone are also defined as nodes. The node density is defined as the total number of nodes per unit area. Then the node density distribution is the distribution of these nodes in any given slice for a given plane. The co-ordination number is defined as the total number of branches or pathways that can be identified for each of the nodes. The distribution of co-ordination number follows a similar definition as the node density distribution. The bond length and its distribution is then the distribution of the actual distance between two connected nodes. Even though the definition of these pore-bond network structure parameters is simple, the actual calculation of these parameters in a complex structure for paper as shown in any of the images is truly challenging.

The skeletonized image of pores, for example, consists of a large two-dimensional matrix of zeros and ones representing each pixel, one being the skeleton and zero being the non-skeleton. The algorithm for node density and co-ordination number determination begins by looking at every pixel to see if it is part of a skeleton. If a pixel is part of the skeleton, i.e. it has an intensity of one, a search is done to see how many individual paths following the skeleton out to the edge of a box surrounding the original pixel can be found. If three or more of these paths are found then this pixel is considered to be a node, and the co-ordination number of the node is equal to the number of individual paths found. In order to avoid counting a node more than once and to avoid clusters of pixels surrounding a node, an artifact of the imaging and skeletonization procedure, a small number of pixels surrounding an identified node is cleared or given an intensity value of zero. A visual comparison of the nodes with the skeleton analysis indicated that this procedure worked quite well in both identifying nodes and eliminating clusters. The node density is found by searching each slice in 40 pixel by 40 pixel segments and then dividing the number of nodes found in each segment by the area of the segment.

A typical average node density distribution and co-ordination number distribution in the XY plane for a slightly refined (670 CSF) and highly refined sample (220 CSF) are shown in Figures 13 thru 16 respectively. As shown in the figures, node density distribution for slightly refined sample appears to be broader with a bigger range than the highly refined sample. A similar behavior was observed in the YZ and XZ planes as well. The frequency

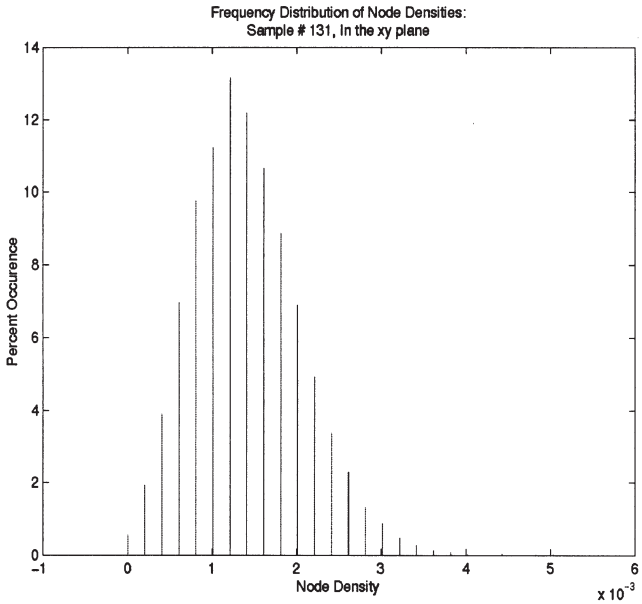

Figure 13 Average node density distribution in the XY plane for unrefined sample.

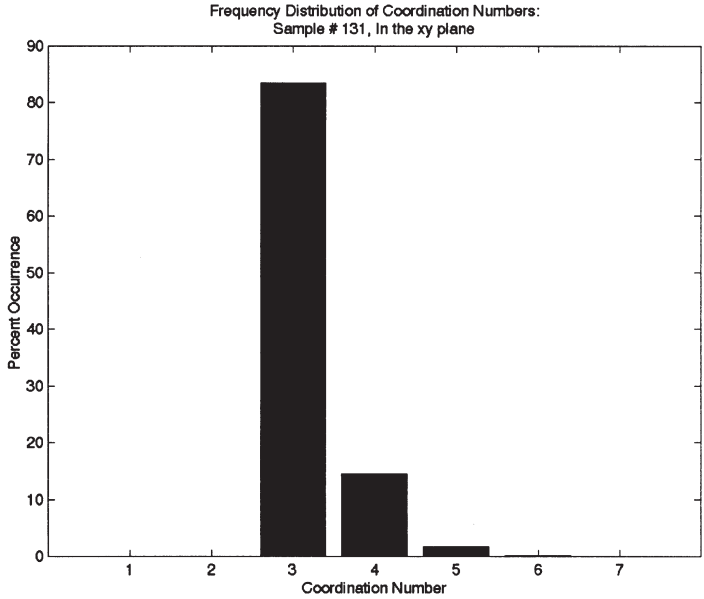

Figure 14 Average co-ordination number distribution in the XY plane for unrefined sample.

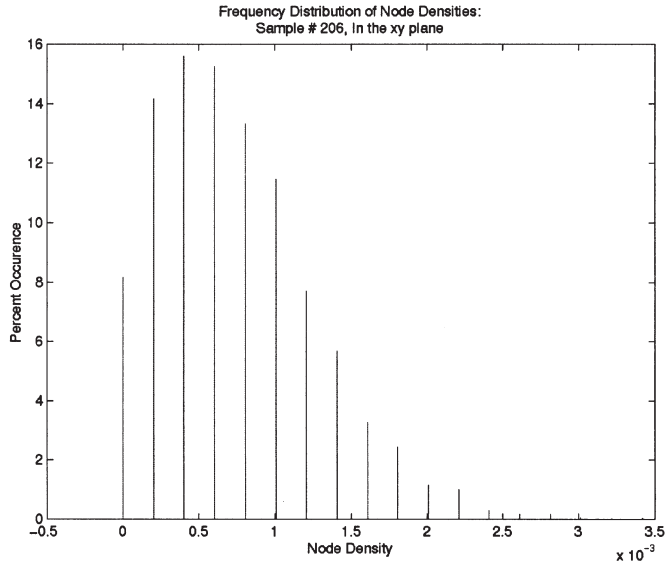

Figure 15 Average node density distribution in the XY plane for highly refined sample.

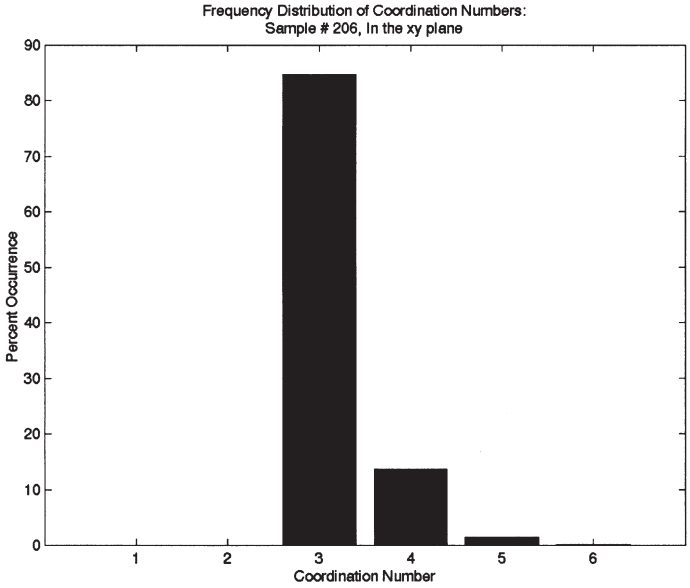

Figure 16 Average co-ordination number distribution in the XY plane for highly refined sample.

distribution of co-ordination numbers appears very similar for the both the sheets. A similar behavior, again, was observed with other planes as well.

A plot of the average node density and co-ordination number for a given plane for the entire thickness of a sample versus freeness shows an interesting behavior (c.f. Figure 17 and Figure 18). Increasing the level of refining or increasing the density of the sheet appear to decrease the average node density and average co-ordination number. This trend is very similar to what was observed with change in porosity and specific surface area with refining. One would expect with refining and higher density sheet, there is a larger number of smaller pores, as shown by pore size distribution. If this were the case then the node density would be expected to increase with refining. On closer observation of the results and the skeletons, it appears that the greater the number of larger pores (as in slightly refined sheet) with more imperfections or rough edges, the skeletonization routine converts this into an image containing long skeleton backbones with many loose branches attached to it. As a result, the node density and the co-ordination number is greater for a slightly refined sheet as compared to a highly refined sheet. This again would be an artifact of the resolution of the X-ray imaging technique. As mentioned earlier, with a higher resolution X-ray technique and employing a smoothing algorithm may solve this problem.

In conclusion, in addition to the traditional methods of describing the void

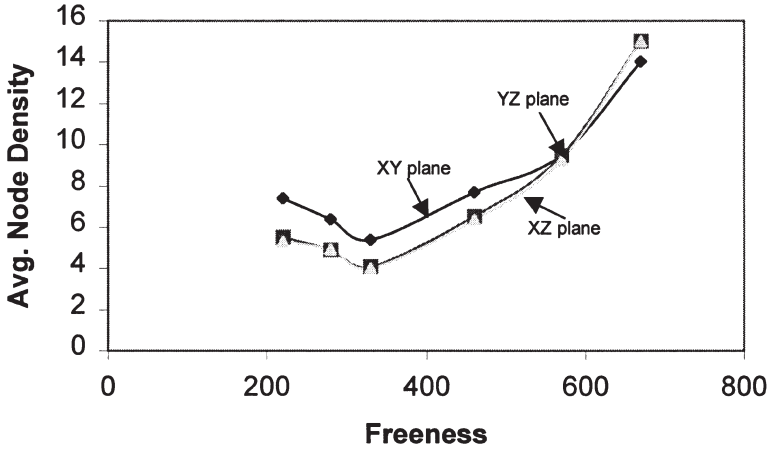

Figure 17 Effect of refining on average node density for all three planes.

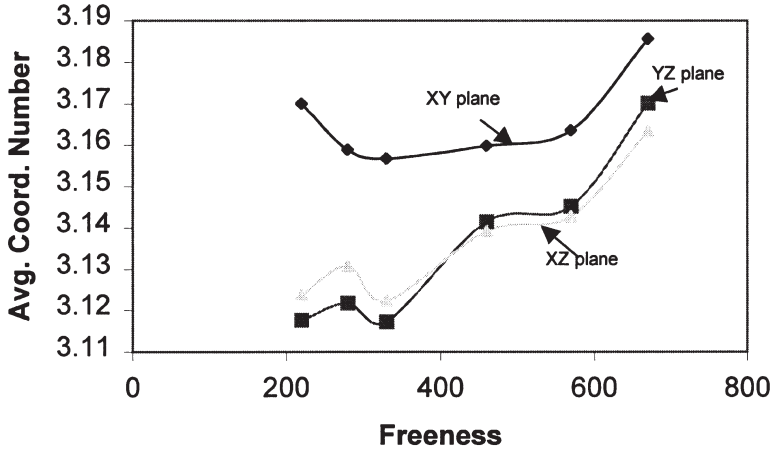

Figure 18 Effect of refining on average co-ordination number for all three planes.

space in paper, the topological complexity can be reflected in morphometric measures including node density, co-ordination number and bond length distributions. The methodology presented here appears to work well even with dense, highly refined sheets. The accuracy of this method can be further improved with a higher resolution X-ray technique. Efforts are underway in obtaining high resolution images and relating pore structure descriptors to liquid and vapor transport.

ACKNOWLEDGEMENT

Partial support of this work by the US Department of Energy, Office of Industrial Technologies, through the Agenda 2020 program in cooperation with the American Forest and Paper Association is acknowledged. Resources provided by Minnesota Supercomputing Institute (MSI) at the University of Minnesota, SkyScan, Belgium (X-ray imaging) and Porous Materials Inc., NY (mercury intrusion porosimetry) are also gratefully acknowledged.

REFERENCES

1. Ramarao, B.V. and Chatterjee, S.G. “Moisture Sorption by Paper Materials Under Varying Humidity Conditions”, in *The Fundamentals of Papermaking Materials* (edited by C. F. Baker), PIRA International, UK, **2**: 703–749 (1997).

2. Bandyopadhyay, A., Radhakrishnan, H., Ramarao, B.V. and Chatterjee, S.G. "Ind. and Engng. Chem. Res. Moisture sorption response of paper subjected to ramp humidity changes", *Modeling and Experiments*, **39** (1): 219–226 (2000).
3. Serra, J., *Image Analysis and Mathematical Morphology*, Vols. I and II. Academic Press, New York (1986).
4. Wang, J.Z., Dillard D.A. and Kamke, F.A. "Transient Moisture Effects in Materials", *J. Mat. Sci.*, **26**: 5113–5126 (1991).
5. Habeger C. and Coffin, D. "Accelerated Creep Mechanics: Parts I and II", in *4th International Symposium on Moisture and Creep Effects on Paper, Board and Containers*: (edited by J. F. Bloch), EFPG, France, (1999).
6. Samuelsen, E.J., Gregersen, O.W., Houen, P.J. and Helle, T. "Three-dimensional imaging of paper by use of synchrotron X-ray microtomography", Proc. Tappi International Paper Physics Conference, **307** (1999).
7. Samuelsen, E.J., Gregersen, O.W., Houen P.J. and Helle T. "X-ray microtomography", *J. Pulp Pap. Sci.*, **27** (2) (2001).
8. Gureyev, T., Evans, R. Stevenson, A.W., Gao, D. and Wilkins, S.W. "X-ray phase contrast microscopy of paper", *Tappi J.*, **84** (2): (2001).
9. Chow, C. K. and Kaneko, T. "Boundary detection of radiographic images by a threshold method", *Information Processing*, **71**: 1529 (1972).
10. Kittler, J. and Illingworth, J. "Minimum error thresholding", *Pattern Recognition,* **19** (1): 41–47 (1986).
11. *Analysis by Porous Materials Inc*., Ithaca, NY, USA.
12. Goel, A., Tzanakakis, M., Huang, S., Ramaswamy, S., Choi, D. and Ramarao, B.V., "Characterization of the three-dimensional structure of paper using X-ray microtomography", *Tappi J*., **84**(5): (2001).
13. Goel, A., Tzanakakis, E.S., Huang, S., Ramaswamy, S., Hu, W.S., Choi, D. and Ramarao, B.V., "Confocal laser scanning microscopy to visualize and characterize the structure of paper" *AICHE Symposium Series*, No. 324, **96**: 75–79 (2000).

Transcription of Discussion

THE 3D STRUCTURE OF PAPER AND ITS RELATIONSHIP TO MOISTURE TRANSPORT IN LIQUID AND VAPOR FORMS

Shri Ramaswamy[1], *Shuiyuan Huang*[1], *Amit Goel*[1], *Aron Cooper*[1], *Doeung Choi*[2], *A. Bandyopadhyay*[3] *and B.V. Ramarao*[3]

[1]Department of Wood and Paper Science, University of Minnesota
[2]Hercules Research Center, Hercules Inc.
[3]SUNY College of Environmental Science and Forestry

Additional Data to the above paper

See following pages

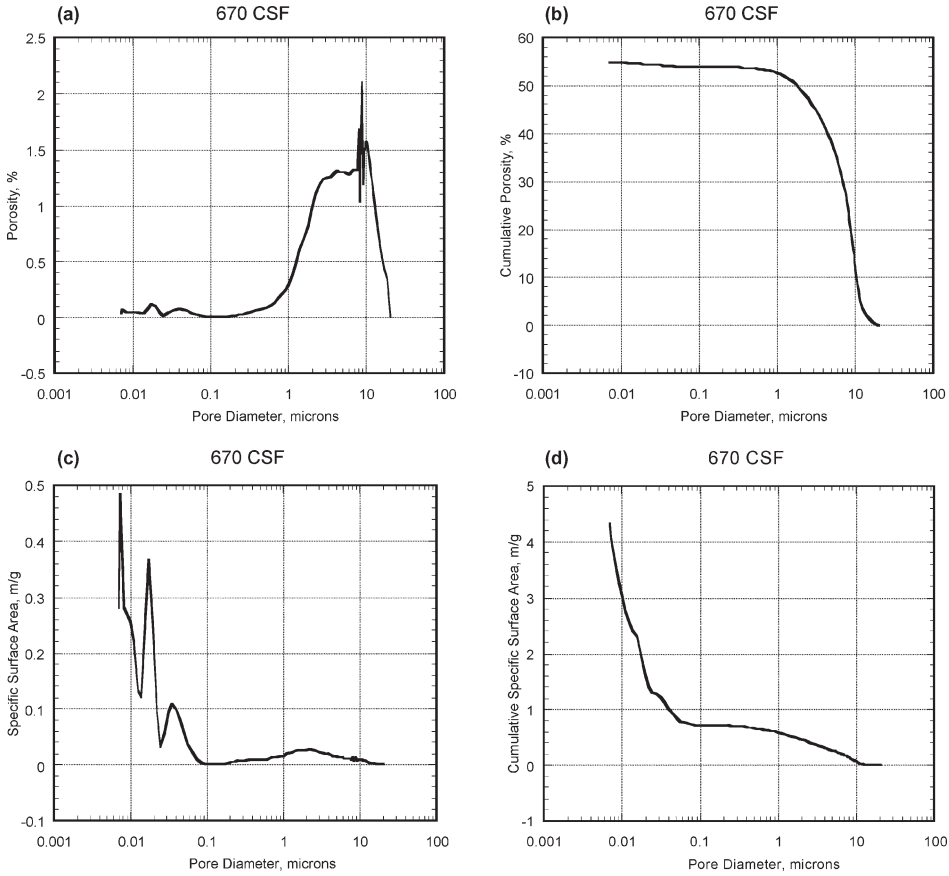

Figure 7 Porosity (a), Cumulative Porosity (b), Specific Surface Area (c), and Cumulative Specific Surface Area (d) distributions by Mercury Intrusion Porosimetry for 670 CSF sample.

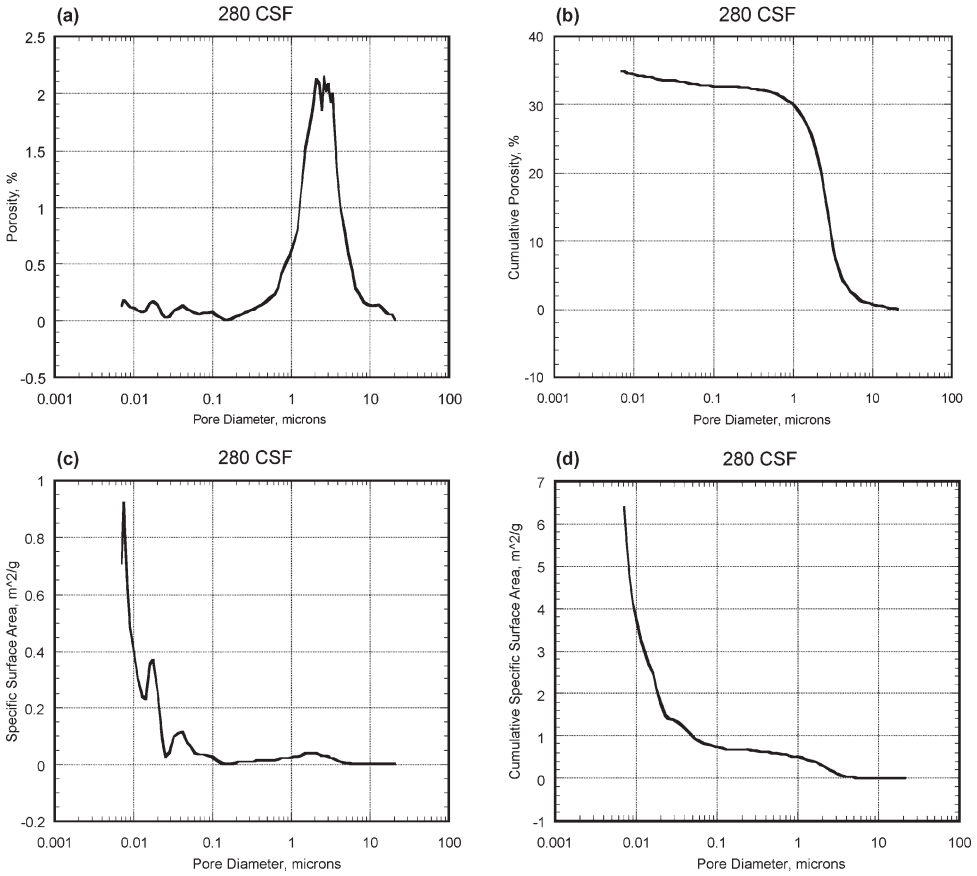

Figure 8 Porosity (a), Cumulative Porosity (b), Specific Surface Area (c), and Cumulative Specific Surface Area (d) distributions by Mercury Intrusion Porosimetry for 280 CSF sample.

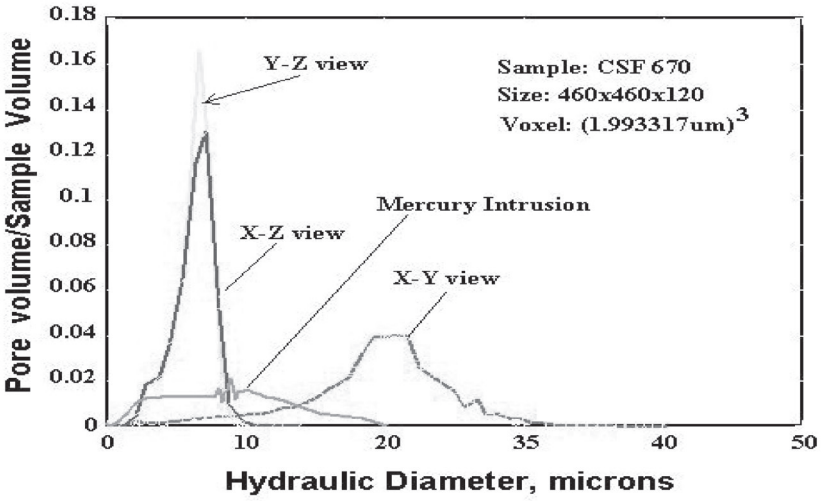

Figure 9 Comparison of pore size distribution in the XY, YZ and XZ planes by image analysis and the mercury intrusion porosimtery for unrefined pulp (670 CSF).

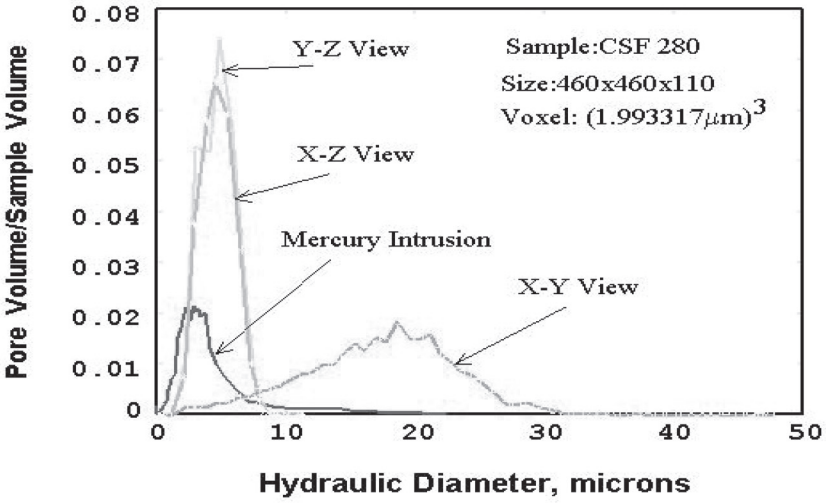

Figure 10 Comparison of pore size distribution in the XY, YZ and XZ planes by image analysis and the mercury intrusion porosimetry for highly refined pulp (280 CSF).

Tortuosity

In addition to classical structure parameters such as porosity, fiber-void interfacial area (surface area) and pore size distribution, one of the other structure descriptor is tortuosity. Tortuosity is defined as the ratio of the actual length of the capillary to the straight line (or the shortest length) length of the capillary. In porous materials such as paper and paperboard, the inter-fiber capillaries can be expected to be highly tortuous. Measurements of tortuosity on a small local scale i.e. between adjacent slices in X-ray images is not very meaningful as the pores are indeed straight on such smaller scale. Then we developed an algorithm to characterize tortuosity for the bulk sample. This algorithm is based on letting tracers (particles) pass through the pores in an actual image of the sample. Starting off on one face of the sample image, the tracers are allowed to traverse through the structure predominantly in a prior decided direction, i.e. in-plane and transverse directions. For example, if the tracer is at some intermediate point in the structure the next step it will take will be in the predominant direction, if that is possible, i.e. if the next voxel in the predominant direction is a pore voxel. If it is not a pore voxel, then a side step will be taken. If none of the other directions are possible, other than the direction that was taken to come into the current pore, then this will be considered a dead pore and the tracer traverse will be stopped and new tracer is begun from the original face of the image. Since the predominant direction can either be in-plane or transverse, it is possible to obtain independent measurements of in-plane and transverse tortuosity.

Figure 19 and Figure 20 show the trajectory followed by sample tracers as they move through the pore structure in the in-plane and transverse directions. It is interesting to note that in some locations the tracer makes a zigzag pattern while trying to find a way out in the predominant direction. Obviously, due to the complex nature of the 3D pore structure of paper and paperboard, one would expect different values of tortuosity for each tracer. Indeed average values of tortuosity with 10,100 tracers were quite different. Then continuing this exercise further we found that if the number of tracers were equal or greater than 1000, then the average values of tortuosity were approximately the same. The average distribution of in-plane and transverse tortuosity values for 1000 tracers for slightly refined sample is shown in Figure 21. As mentioned before, the transverse tortuosity is always greater than in-plane tortuosity. Also, it is interesting to note that the transverse tortuosity has a wider distribution suggesting broader range of tortuosity values.

This exercise was then carried out for six different samples of varying refining levels and structure. The plot of transverse and in-plane tortuosity versus refining or freeness is shown in Figure 22. It is interesting that for all

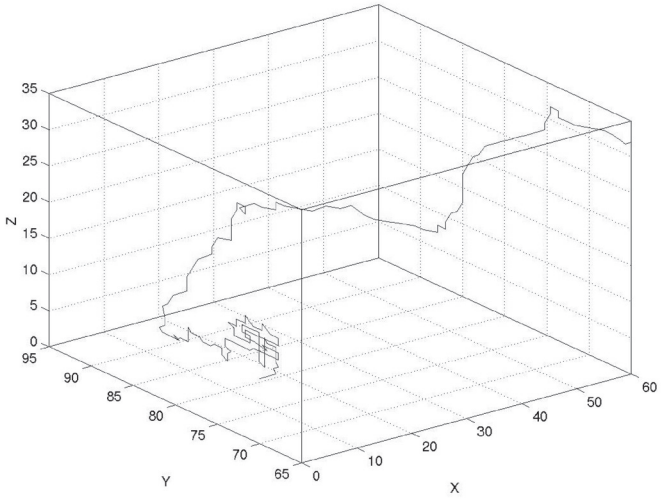

Figure 19 Trajectory followed by sample tracer through the pore structure in the in-plane direction

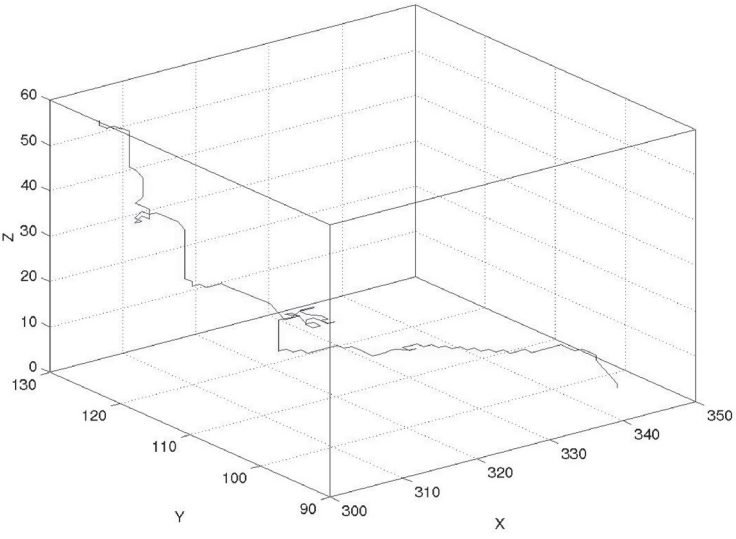

Figure 20 Trajectory followed by sample tracer through the pore structure in the transverse direction

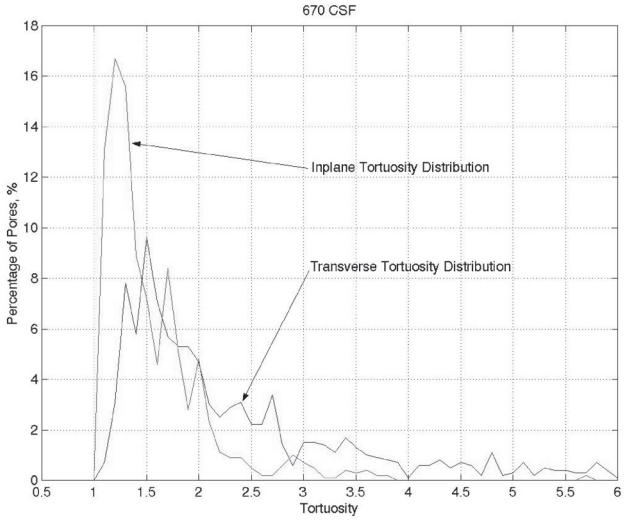

Figure 21 In-plane versus transverse tortuosity distribution for slightly refined sample (670 CSF) (average of 1000 tracers for each direction)

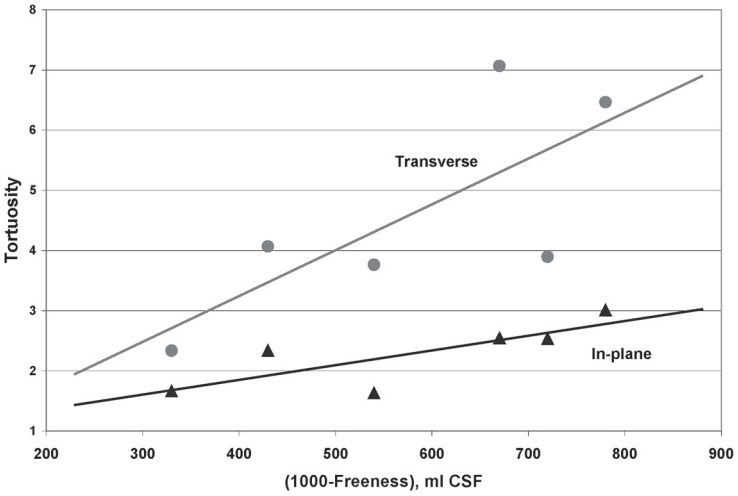

Figure 22 Effect of refining on average in-plane and transverse tortuosity (average of 1000 tracers for each direction)

refining levels the transverse tortuosity is always greater than in-plane tortuosity. Also, the difference between in-plane and transverse tortuosity increases as the sheet is more refined. This along with differences in pore size distribution may help explain the observed differences in in-plane versus transverse liquid permeability and vapor diffusivity.

Peter Matthews University of Plymouth

Can I refer you back to three of your figures in Volume 2, Page 1302, Figures 9 and 10; these are the figures where you have the mercury intrusion data. You notice on Figure 9 that mercury intrusion data is spread right across your two pore size distribution. If you go to Figure 10, you notice that the mercury intrusion data is now only revealing the smaller sizes of void. That suggests in that particular sample, your highly refined pulp sample, the larger voids are being shielded by smaller connections. The mercury intrusion is only showing up the small voids, therefore for the mercury intrusion the larger voids are being shielded i.e. they are surrounded by small voids.

Shri Ramaswamy

If the larger pores are not directly accessible then I would expect, lets say if you have a throat with a very small dimension and then at the bottom of it you have a large pore, if the mercury cannot get through the small pore then obviously the large pore volume was undetected.

Peter Matthews

That actually agrees with your conclusions later on where you are saying that some of the results might be an artefact of your measurements, and your conclusions later on, Figure 18. I am just saying that those comparisons may be an important effect in terms of the structure. In turn you may be able to get something quite important about the fluid transport characteristics through that structure; the absorbtion characteristics and so on.

Shri Ramaswamy

One of things that I have been thinking of doing is that if I have a tracer which is moving through the structure every time it take a step we look at

what pore it is part of, and what is the diameter of that pore. If a tracer can get through a surface it is big enough if the opening is enough for one pixal or voxal to go through. If I have a 6 micron pore converging down to 1 micron every time I take a step I look at the diameter of my pore I can exactly find out if it is narrowing down and how many throats there are in my whole structure.

Peter Matthews

Yes but even without any of the modelling whatsoever, simply by looking at that diagram and the previous diagram you may be able to pull out something quite important.

Shri Ramaswamy

Another thing is that the pore correction that you mentioned is something that we have not taken into account. That again may change this comparison.

Mark Knackstedt Australian National University

I come from the petroleum area and there we know photomicrographs and mercury porosimetry give very different pore sizes, in fact different by an order of magnitude. You are getting a match and looking at your paper I can't understand why. Especially if you look at your data you've got in the xz view a hydraulic diameter of about 2 to 4 microns. According to your voxel size that means most of the pores in cross section, if I looked in the xz or yz view, would actually only be 1 or 2 voxels wide, so I would have almost a speckled pattern. If you look at your images they don't look like tiny pores in fact they are broached by about 10 or 20 voxels. So why if I look at it in-plane am I seeing much larger pores than you are showing here?

Shri Ramaswamy

I think that was just one sample image from an unrefined sample. If you look at multiple images from our structures you do see smaller size pores

Mark Knackstedt

So you are telling me that you have an almost fractal rough surface? So you haven't smoothed your surface?

Discussion

Shri Ramaswamy

No we haven't smoothed our surface in this analysis.

Mark Knackstedt

Which is actually an artefact probably of the image.

Shri Ramaswamy

Yes absolutely especially if you go to a 1 micron resolution image, and, we further smooth out our surface, we may get improved information.